Orbital mixing and strong Hund's coupling stabilize spin order in the van der Waals ferromagnet CrI_3

A. De Vita,[1,2,*] S. Stavrić,[3,†] R. Sant,[4,5] N. B. Brookes,[4] I. Vobornik,[6] G. Panaccione,[6] S. Picozzi,[7,8] M. Wolf,[2] L. Rettig,[2] R. Ernstorfer,[1,2,‡] and T. Pincelli[1,2,§]

[1]*Institut für Physik und Astronomie, Technische Universität Berlin, Straße des 17 Juni 135, 10623 Berlin, Germany*
[2]*Fritz Haber Institute of the Max Planck Society, Faradayweg 4-6, 14195 Berlin, Germany*
[3]*Vinča Institute of Nuclear Sciences–National Institute of the Republic of Serbia, University of Belgrade, P.O. Box 522, RS-11001 Belgrade, Serbia*
[4]*ESRF, The European Synchrotron, 71 Avenue des Martyrs, CS40220, 38043 Grenoble Cedex 9, France*
[5]*Dipartimento di Fisica, Politecnico di Milano, Piazza Leonardo da Vinci 32, I-20133 Milano, Italy*
[6]*Consiglio Nazionale delle Ricerche CNR-IOM, Unità di Trieste, Strada Statale 14, km 163.5, 34149 Basovizza (TS), Italy*
[7]*Department of Materials Science, University of Milan-Bicocca, Via Roberto Cozzi 55, 20125 Milan, Italy*
[8]*Consiglio Nazionale delle Ricerche CNR-SPIN, c/o Università degli Studi 'G. D'Annunzio,' 66100 Chieti, Italy*

(Received 12 January 2026; revised 27 March 2026; accepted 7 April 2026; published 8 May 2026)

Recent years have seen a vast increase in research into van der Waals magnetic materials. In many of these systems, magnetism is introduced via light $3d$ transition metal elements, combined with chalcogenides or halogens. Despite the great technological promise in the field of spintronics, the connection between the d-orbital configuration and the occurrence of low-dimensional magnetic order is currently unclear. Here we address the prototypical two-dimensional ferromagnet CrI_3, via complementary spectroscopies and density functional theory calculations. We reveal the electronic structure and orbital character of bulk CrI_3 in the paramagnetic and ferromagnetic phases, describing the couplings underpinning its energy diagram, and providing a robust experimental demonstration that the stabilization of ferromagnetism is attributable to orbital mixing between I p and Cr e_g states, and to the presence of strong Hund's coupling. These findings reveal the microscopic connection between orbital and spin degrees of freedom, providing fundamental insights into the behavior of low-dimensional magnetic materials.

DOI: 10.1103/bdbj-98tj

I. INTRODUCTION

Van der Waals (vdW) magnets constitute a versatile platform where exotic quantum states can be realized in view of applications in spin- and orbitronics [1–3]. In particular, much interest has been drawn to the orbital degree of freedom in quantum materials [4–6]. Given the dimensional confinement in vdW layers, a working approximation of localized, orbitally pure electronic states would seem adequate. On the other hand, orbital-specific correlations and couplings are significant to solve ground state and collective excitations in these systems [7–9]. Understanding the interplay between orbital occupation and electronic ordering, as well as the d-electron contribution to the emergence of low-dimensionality magnetism, represents a fundamental research challenge.

Among vdW magnets, the layered ferromagnet CrI_3 exhibits long-range magnetism down to the monolayer limit induced by magnetic anisotropy, with stacking-dependent magnetic order and a pronounced magnetoelectric response [10–17]. This makes CrI_3 an ideal candidate to probe the influence of orbital phenomena on the magnetic configuration. In particular, Kim *et al.* [18] have proposed that the stabilization of magnetic interactions in CrI_3 involves a strong contribution originating from p-d covalency. While this proposition has been well received, few spectroscopic studies have been aimed at providing a detailed experimental investigation, mostly limited to the nonmagnetic phase of CrI_3 due to its extreme hygroscopicity, sensitivity to contamination, and charging at low temperatures [19,20].

In this work, we present a multifaceted study of the electronic structure of CrI_3 above and below the Curie temperature $T_C = 61$ K, combining Angle-Resolved Photoemission Spectroscopy (ARPES) and X-ray Magnetic Circular Dichroism (XMCD) with density functional theory (DFT) and multiplet cluster calculations. Absorption data demonstrate that CrI_3 displays a covalent character caused by orbital mixing between Cr e_g and I $5p$ states. Electronic band structure modifications attributed to exchange-induced splitting and Hund's energy gain were detected by temperature-dependent ARPES and supported by DFT calculations. The combined techniques

*Contact author: alessandro.de.vita@tu-berlin.de
†Contact author: stavric@vin.bg.ac.rs
‡Contact author: ernstorfer@tu-berlin.de
§Contact author: pincelli@tu-berlin.de

Published by the American Physical Society under the terms of the Creative Commons Attribution 4.0 International license. Further distribution of this work must maintain attribution to the author(s) and the published article's title, journal citation, and DOI.

bring robust experimental proof that the Cr-I hybridization is responsible for the stabilization of ferromagnetism in CrI_3, and establishes the role of Hund's coupling as a major driving force in this system. Our findings provide essential information on the electronic structure of this material, and offer insight on the microscopic orbital mechanisms underpinning its properties.

II. METHODS

A. Photoelectron spectroscopy

ARPES spectra have been acquired with XUV *p*-polarized photons at 21.7 eV, provided by the high-harmonics generation setup in the ARPES laboratory at the Fritz Haber Institute of the Max Planck Society, Berlin [21,22]. The overall energy resolution has been estimated to be ≈150 m eV; the spot size is 80 μm FWHM. Commercially available CrI_3 crystals have been mounted on sample holders while in N_2 atmosphere and low, red light conditions using silver epoxy glue (HD20E, Epotek), and cleaved in UHV ($p < 8 \times 10^{-11}$ mbar) before the measurement. To compensate for sample charging at low temperatures, a 400 nm, continuous wave (CW) laser has been used in conjunction with XUV during the measurement. Like the similar halide VI_3 [23], CrI_3 displays pronounced light sensitivity under beam: for this reason, we monitored the peaks at −1.3 and −2 eV as proxies to spot variations in the line shape as a function of measurement time. Since the beam footprint on the sample surface is roughly 50 μm × 100 μm, any beam damage is a local effect, and moving to another spot generally recovers the initial line shape. Compared to VI_3, CrI_3 is somewhat more sensitive to irradiation, therefore surface degradation from adsorbates cannot be effectively countered by increasing the photon flux. (*E*,*k*) spectra have been collected with a time-of-flight (TOF) momentum microscope at 65° incidence angle and normal emission conditions.

Resonant-ARPES measurements at resonant photon energy have been acquired at the APE-LE beamline of the Elettra Synchrotron Radiation Facility [24]. CrI_3 crystals have been mounted on sample holders while in N_2 atmosphere using silver epoxy glue (HD20E, Epotek), and cleaved in a pressure better than 5×10^{-9} mbar before the measurement. Samples were aligned with the slit along the $\bar{\Gamma}$-$\bar{K}$ direction, and kept at 45° incidence angle and normal emission conditions.

The energy axis in all the (*E*,*k*) spectra has been aligned such that the valence band maximum (VBM) corresponds to zero energy. We employed a standard approach in semiconductor physics, as described in Refs. [25,26]: we linearly extrapolate the spectral leading edge to the baseline, and take the intersection as a proxy for VBM. An example energy distribution curve (EDC) is shown in Supplemental Material, Fig. S1 [27].

B. Absorption spectroscopy

X-ray absorption spectroscopy (XAS) and XMCD measurements have been acquired at beamline ID32 of the European Synchrotron Research Facility [28,29]. Commercially available CrI_3 crystals stored in Ar atmosphere (<0.5 ppm O_2, <0.5 ppm H_2O) have been transferred in inert static atmosphere and cleaved under N_2 flow inside the loadlock chamber, to expose the (0001) crystallographic plane of the clean surface avoiding oxidation of the highly hygroscopic surface due to moisture; the sample was held in UHV (pressure $<3 \times 10^{-10}$ mbar). XAS spectra have been acquired in total electron yield at normal incidence and normalized by the intensity collected on a Au mesh in front of the sample stage. The beam has almost 100% degree of linear and circular polarization, and the setup has resolving power better than 5000. A Cr_2O_3 calibration sample located after the exit slit [29] has been used as reference for the energy scale. XMCD spectra are the difference between left- and right-circularly polarized light spectra, measured at remanence after zero-field cooling from room temperature to 25 K following application of a 0.5-T out-of-plane magnetic field. Measurements have been performed at 30 and 90 K. The beam spot diameter at sample position at normal incidence is 100 μm × 100 μm.

C. DFT calculations

DFT calculations were performed by using the Vienna *Ab initio* Simulation Package (VASP) [30–32]. The lattice constant of $a = 6.817$ Å and a Cr–I bond length of 2.689 Å were determined by performing the spin-polarized relaxation of the monolayer structure in the ferromagnetic state using the PBEsol exchange-correlation functional [33]. A plane-wave energy cutoff of 350 eV was used, and the Brillouin zone (BZ) was sampled with a 24×24×1 *k*-point grid. To treat the Cr 3*d* states, we adopted the DFT+*U* approach as introduced by Liechtenstein *et al.* [34], and tested several Hubbard *U* and Hund *J* values to find the best agreement between experiments (details on the particular choice of *U* and *J* parameters are given below). Since the I 5*p*-dominated VBM states are important to our analysis and given iodine's strong spin-orbit coupling (SOC) effects [note that $Z(\mathrm{I}) = 53$], we included SOC with noncollinear DFT to properly describe these states. Notably, including SOC has minimal influence on the energy positions of the deeper Cr 3*d* states.

III. MAIN TEXT

The (low-temperature) rhombohedral ($R\bar{3}$) crystal structure [35], bulk and surface Brillouin zone (BZ), as well as the nominal Cr 3*d* orbital filling are depicted in Figs. 1(a)–1(c). Firstly, we consider ARPES data obtained on the CrI_3 valence band (VB) at $T = 300$ K. The isoenergetic surface and the (*E*,*k*) spectra along the high-symmetry directions in the surface BZ are presented in Figs. 1(d) and 1(e). Measurements are consistent with previous results [20]: the VBM is dominated by strongly dispersive states, displaying a slight trigonal warping [Fig. 1(d)], whereas at higher binding energies (BEs) from −1 to −2 eV the electronic states appear more localized.

We model the CrI_3 electronic structure using noncollinear DFT with SOC included. Due to the vdW nature of bulk CrI_3 and the presence of SOC-induced anisotropy, the band structure evolution across the magnetic phase transition is dominated by intralayer interactions, with interlayer effects playing a secondary role. We therefore model CrI_3 as a monolayer. The paramagnetic (PM) state is reproduced by using

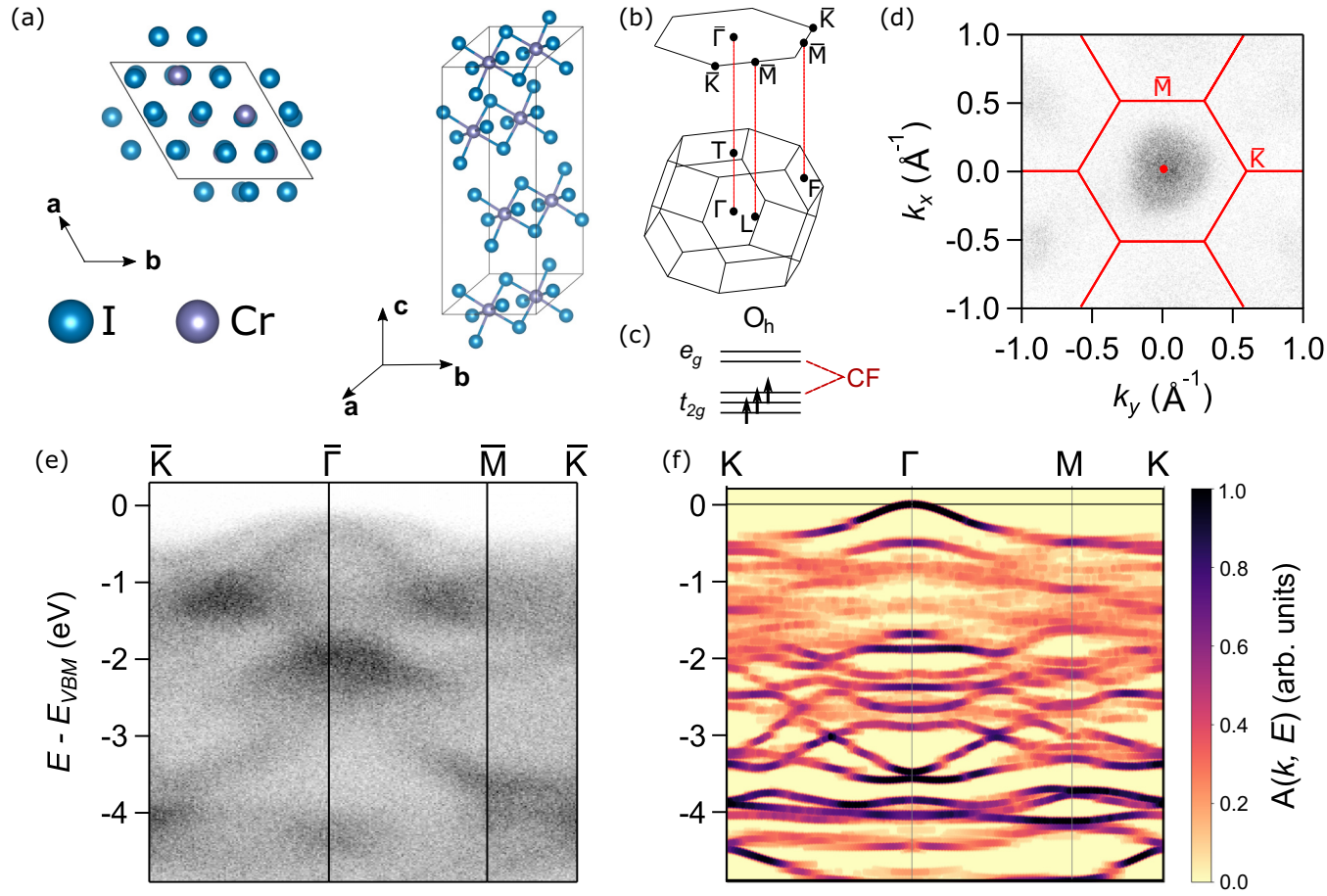


FIG. 1. (a) Top and side hard-sphere view of theCrI$_3$ crystal structure, where each Cr center is coordinated by six I atoms. (b) Bulk first Brillouin zone of CrI$_3$ and corresponding surface projection; high-symmetry points are indicated in both cases. (c) Crystal field splitting and nominal electron filling for O$_h$ symmetry. (d) Photoemission intensity (grayscale; darker represents higher electron count) of the isoenergetic (k_x,k_y) surface at $E - E_{\mathrm{VBM}} = -0.1$ eV, at $h\nu = 21.7$ eV photon energy and $T = 300$ K. The red overlay highlights high-symmetry points and lines. (e) ARPES (E,k) spectrum of the CrI$_3$ valence band dispersion along high-symmetry lines in the same experimental conditions as (d). (f) The spectral function $A(\mathbf{k}, E)$ of the paramagnetic state calculated with DFT.

the $3 \times 3 \times 1$ supercell and introducing magnetic disorder through the special quasirandom structures (SQS) method [36,37] (see the Appendix for technical details). To reveal how disordering of Cr magnetic moments affects the electronic bands across different energy ranges, we compute the spectral function $A(\mathbf{k}, E)$ and unfold it to the unit cell [38] to enable direct comparison with ARPES data. We systematically evaluate various Hubbard U and Hund J parameters for the Cr $3d$ orbitals, ultimately determining that $U = 1.3$ eV and $J = 0.9$ eV yield optimal agreement of the calculated spectral function with ARPES measurements in terms of band dispersion at the VBM, high-intensity pockets between -1 and -2 eV, and other features at higher BEs [Figs. 1(e) and 1(f)]. We note that the (U, J) parameters were calibrated by tracking the energy position of the occupied Cr $3d$ band maxima rather than the band-gap magnitude, which is often the standard metric in combined experimental-computational studies. This approach is necessitated by the insensitivity of the CrI$_3$ band gap to the Hubbard U and J values. Specifically, the valence band maximum consists primarily of I $5p$ states, while the conduction band minimum is composed of spin-majority Cr $3d$ states, both of which are largely unaffected by the local Hubbard interaction on the Cr sites. Notwithstanding this insensitivity, our selected (U, J) values yield a DFT band gap of 1.22 eV in the ferromagnetic (FM) state and 1.27 eV in the PM state, values that are in excellent agreement with previously reported calculations and the experimental optical gap of $\sim$1.2 eV [39–42]. Spectral functions calculated with different (U, J) parameters are presented in Fig. S6. Flat bands around Γ appearing at -2 eV in Fig. 1(e) are well captured by DFT, as well as the bundle of bands at -4 eV spreading throughout the BZ. While the energy positions of bands can be compared between ARPES measurements and DFT-calculated spectral functions, their intensities can be only partly related, because the DFT-calculated spectral function does not reproduce the intensity nuance of the ARPES signal arising from many-body interactions and Bloch wave-function symmetries.

To further assess how the charge distribution affects the VB, we acquired ARPES spectra out of and at resonance with the Cr $3p$ core level, displayed in Fig. 2(a). At resonance, the nondispersive feature centered at ~ -1.3 eV is strongly enhanced, as emphasized also by the corresponding EDCs in Fig. 2(b). We attribute this manifold to states with

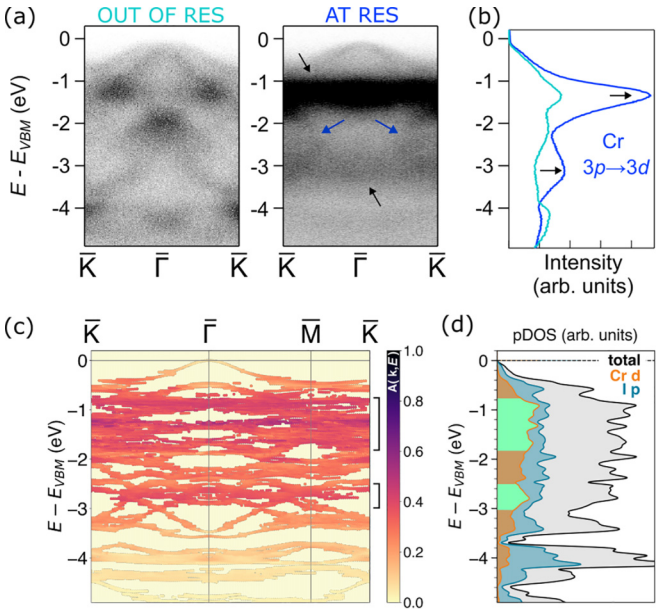


FIG. 2. (a) ARPES (E,k) spectra along the $\bar{K}$-$\bar{\Gamma}$-$\bar{K}$ direction, at 21.7 eV (left, out of resonance) and 49 eV (right, at resonance), at 300 K. Black and blue arrows point at the features with increased spectral weight. (b) k-integrated EDCs of the spectra in (a): out of resonance is teal; at resonance is blue. Black arrows mark the two prominent increases in intensity. (c) Cr 3d bands calculated with DFT in the PM state. (d) Atomic-orbital projected density of states in the PM state. Areas shaded in green highlight the local maxima of Cr 3d states, as described in the main text.

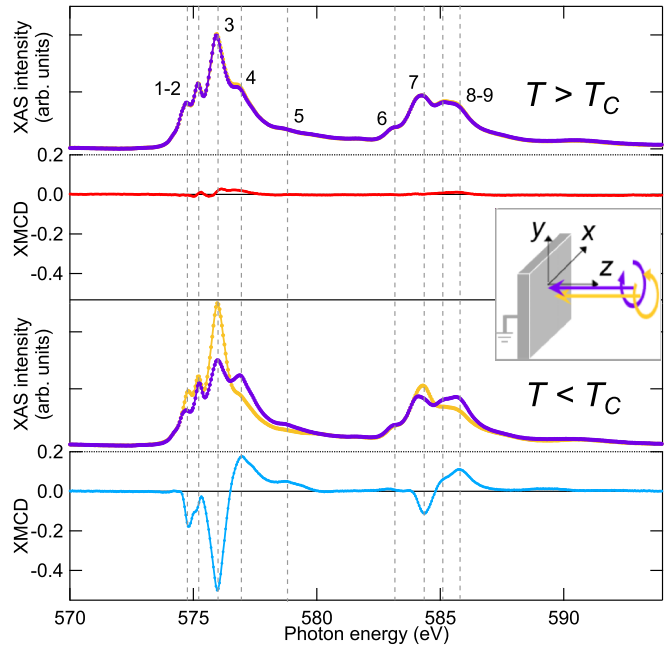


FIG. 3. XAS spectra across the Cr $L^{2,3}$ edges, acquired with left- and right-circularly polarized photons, and corresponding XMCD, at 90 K (top) and at 30 K (bottom). The inset shows the experimental geometry.

Cr 3d character, as observed also in Ref. [20] in a photon energy scan across the whole Cr 3p absorption edge. Additionally, a weakly dispersing feature at ~ -3.1 eV, as well as two arms of an electronlike dispersive band at the edge of the BZ from -1.5 to -3 eV [highlighted by blue arrows in Fig. 2(a)], appear enhanced at resonance. While the former gives a well-defined peak in the corresponding EDC, the intensity of the latter contributes to the whole energy range from -1.5 to -3 eV, therefore no corresponding peak can be identified. Differently from the state at ~ -1.3 eV, our out-of-resonance data do not reveal these other states at all, probably because of unfavorable matrix elements suppressing the photoemitted intensity. The difference in spectral weight of the bright bands at resonance is also likely due to photoemission matrix elements, preventing us from revealing the whole extent of the Cr d-orbital manifold in the valence band with uniform intensity.

To facilitate comparison between ARPES measurements and the DFT-calculated spectral function, in Fig. 2(c) we projected the Cr 3d bands from the total spectral function shown in Fig. 1(f). To show the number of electronic states at different energies more transparently, we display the atom-projected density of states (pDOS) side by side with the spectral function. From this plot we can observe that the Cr 3d and I 5p states overlap in a broad range across several electronvolts, suggesting strong orbital mixing between the two. Cr 3d states span from the VBM down to -3.6 eV, displaying two distinct features: a larger (broader) one centered around -1.3 eV and a smaller (narrower) one at -2.8 eV [green highlight in Fig. 2(d)]. When the intensity and energy positions of these features are compared to the EDCs acquired at 300 K [Fig. 2(b)], they correspond to regions of high spectral weight arising from the Cr 3d bands at -1.3 and -3.1 eV. Moreover, the distributed intensity between the two local maxima mirrors the presence of the dispersive states from -1.5 to -3 eV. We emphasize that the right choice of Hubbard U on Cr 3d orbitals is crucial here, as the higher U values push down the larger feature too much, so that for $U > 2.0$ eV the two features merge into a single broad band (Fig. S7).

Unlike these deeper states that come mostly from Cr 3d orbitals, the states just below the VBM are mainly derived from I 5p orbitals. This can be rationalized from the disappearance of the prominent dispersing band at the VBM near Γ [Fig. 1(f)] in the Cr 3d-projected spectral function [Fig. 2(c)]. Additionally, the very deep states between -3.8 and -4.6 eV, clearly visible in off-resonance ARPES measurements and suppressed under resonant conditions [Fig 3(a)], exhibit almost exclusively I 5p character, which is evident from the pDOS plot in Fig. 2(d).

Now we turn to the orbital character in the ferromagnetic state of CrI_3. We present in Fig. 3 the XAS and XMCD spectra across the Cr $L_{2,3}$ edges, below and above T_C. The overall line shape of the XAS white line [18,43] shows the main L_3 peak (3) at 575.9 eV; two features lie at lower (peaks 1,2) and higher (peaks 4,5) photon energies. The L_2 peak displays two features giving opposite dichroism (7,9), with a minor peak of the same dichroic character (8) and a preedge (6). We also observe almost no difference between $T > T_C$ and $T < T_C$ in the line shape of the polarization-averaged XAS spectra (Supplemental Material Fig. S2, main panel), which

suggests that sample conditions were extremely stable during the measurement, and that the difference in the XMCDs is fully attributable to intrinsic effects.

We quantify from sum rules [44] the orbital and effective spin moments as $m_L = 0.00 \pm 0.06 \mu_B$/Cr and $m_S = 2.45 \pm 0.05 \mu_B$/Cr. The slightly positive measured value of μ_L is smaller than the error, and compatible with zero orbital moment, as expected in CrI_3. Conversely, m_S is somewhat lower than the expected value ($3\mu_B$/Cr). In any case, the calculation of m_L and especially m_S is not necessarily an accurate procedure for early transition metals, due to the large overlap between the L_3 and L_2 edges [45].

To compare our data, we refer to previous results on CrI_3 [43], as well as the standard reference for pure Cr^{3+} valence states, the oxide Cr_2O_3 [46–50], similar to CrI_3 in terms of crystal structure, nominal transition metal valence, and ligand coordination geometry. The details of the line shape and the relative intensity between peaks show clear deviations from Ref. [43], which is in turn closer to Cr_2O_3. Features located in the low-energy region and in the neighborhood of preedges of the L_3 and L_2 peaks, which are crucial to correctly assess the orbital character in transition metal halides [51,52], show the most evident differences. In our case, peak (1) is sharper and more pronounced, peak (2) has no equivalent, and peak (6) emerges more clearly from the preedge region, other than presenting a nonzero dichroic signal. Lastly, the tail of the L_3 peak is considerably less broad.

We also note that the $L_{2,3}$ edges appear shifted towards lower photon energies compared to Cr_2O_3 [46–50], although not strongly enough to justify an outright change in valence state [53]. From these observations we gather that the electronic character in CrI_3 shows an excess of electrons compared to a pure Cr^{3+}. A higher electron count at the cation site in CrI_3 does not necessarily imply a mixed valence state: that would affect the line shape of the XAS white line by considerably broadening spectral features, as seen, e.g., in mixed-valence manganites [54–57]. The small signal in the preedge region around 573 eV (Supplemental Material Fig. S2, inset), where typically Cr^{2+} states are located [53,58,59], is 2 orders of magnitude lower compared to the intensity of the main peaks; not nearly enough to support a mixed-valence state. Instead, we interpret our data as a partial redistribution of the charge by the ligands; that is, a more *covalent* character of the bond due to Cr e_g–I $5p$ orbital hybridization [8,60,61]. This is further supported by the presence of a dichroic signal of the same sign at the I $M_{4,5}$ edges (Supplemental Material, Fig. S3), due to mixing of Cr and I final states [18]. Moreover, multiplet cluster calculations based on the quanty code [62] show that, in the absence of hybridization, several features at the Cr $L_{2,3}$ edges appear at odds with the experiment. If hybridization is taken into account, calculations match our experimental line shape more closely, and we are able to extract a $3d$ electron occupation of $n = 3.52$ (Supplemental Material, Fig. S4 and Table S1). We attribute the high effective Cr $3d$ occupancy to the strong Cr–I covalency, which defines the local chemical environment and effectively increases the electron count on the Cr site.

To assess the modifications induced in the electronic structure by the development of the ferromagnetic ordering, we acquired (E,k) spectra above and below T_C, shown in Fig. 4(a). We extracted EDCs at the $\bar{\Gamma}$ point in Fig. 4(b), to better illustrate the changes occurring in the band dispersion.

By comparing spectra and EDCs, we do not observe significant changes in effective masses within bands, or in the energy position of the features at high BE, indicating that the bandwidth of the VB is not strongly affected. However, two major modifications take place: at $T < T_C$, we can see that (i) the holelike pocket at $\bar{\Gamma}$ at -2 eV, corresponding to the most intense peak in the EDCs in Fig. 4(b) (red arrow), shifts towards higher BEs and broadens, revealing two separate components (blue arrows); and (ii) the VBM area shows a displacement of the two dispersive I $5p$ bands (black arrows), translating into a noticeable broadening in the EDCs.

When looking at the inset in Fig. 4(b), where the VBM region is zoomed in, the cutoff of the EDC at the VBM is sharper at higher temperatures, contrasting with the expected thermal broadening. Similarly, the feature at -2 eV broadens at lower temperature, in contrast with the behavior of bands in other regions of the spectrum (Supplemental Material Fig. S5).

To understand the different spectral contributions, we fitted the EDCs with Gaussian shapes superimposed to a Shirley background, focusing in particular on the region at -2 eV and the VBM [Fig. 4(c)]. The EDC at 300 K shows the presence of two overlapping bands, one much broader than the other, marked by different effective masses as evident from the (E,k) dispersion. On the other hand, at $T = 50$ K two such peaks appear on top of the broader signal. This is consistent with a splitting of ≈450 m eV of the sharper feature in two separate photoemission signals in the FM state. We notice the same effect at the VBM, where a splitting appears (≈250 m eV). It is also noteworthy that the center of mass of the I $5p$ band manifold at -2 eV shifts towards lower BEs by ≈300 m eV. On the other hand, the shifts of other bands are comparable to our experimental bandwidth (≈100 m eV), therefore no conclusive statement can be made.

The experimental EDC spectra are further interpreted through the lens of DFT-calculated pDOS evaluated at the Γ point. Figure 4(d) shows how selected single peaks in the PM phase each split into two in the FM phase (small black arrows). The peak at the VBM is of purely I $5p$ character, whereas the feature situated at approximately -0.6 eV consists of hybridized spin-majority Cr $3d$ and I $5p$ states. In the FM phase, both peaks exhibit an exchange splitting of roughly 100 m eV. Given the purely I $5p$ nature of the VBM, this observation strongly suggests that the ferromagnetic alignment of the Cr magnetic moments, mediated via Cr e_g–I $5p$ hybridization channels, is highly efficient in splitting the iodine states.

For the deeper states in the EDC spectra—specifically the single peak near -2 eV in the PM phase that splits into two features in the FM phase [Fig. 4(c)]—the interpretation is less straightforward. In this energy range (-1.5 to -3.0 eV), the DFT-calculated pDOS contains several overlapping contributions, which makes a quantitative determination of the splitting difficult.

Symmetry considerations further support that the long-range magnetic ordering in the FM ground state is precisely driven by the orbital mixing. The only symmetry-allowed ligand-to-metal bonds are σ type involving e_g and π type

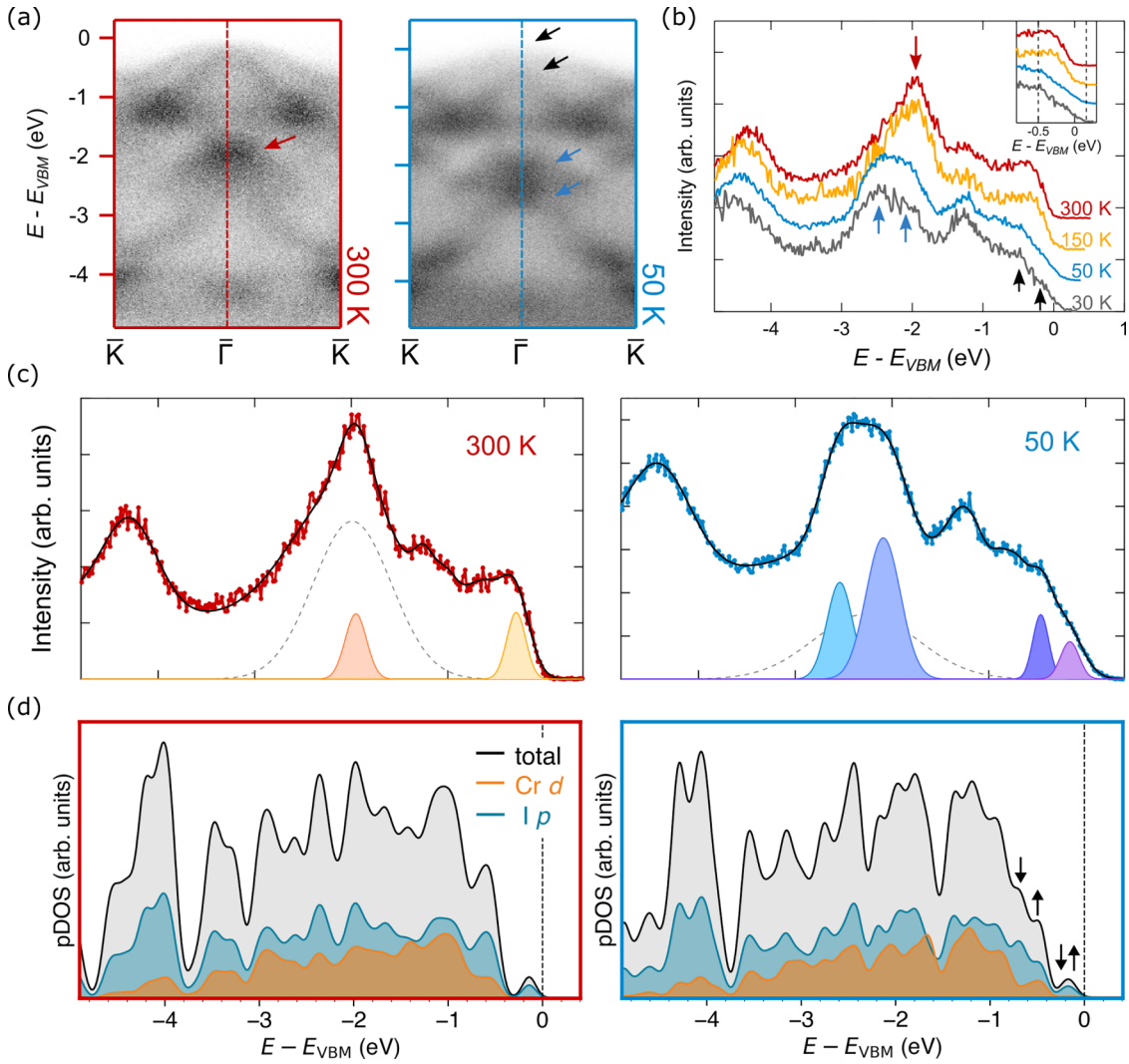


FIG. 4. (a) ARPES (E,k) spectra along the $\bar{K}$-$\bar{\Gamma}$-$\bar{K}$ direction, at $T = 300$ K and $T = 30$ K. (b) EDCs at $\bar{\Gamma}$ as a function of temperature. The inset enhances the VBM region to highlight the change in slope. (c) EDCs at $\bar{\Gamma}$ at 300 K (left) and at 50 K (right). The black line is a multipeak fit as described in the main text. The colored Gaussians represent the spectral features splitting below T_C. (d) Calculated pDOS at the Γ point, including 100 m eV Gaussian broadening to account for experimental resolution, in the PM (left) and FM (right) phases projected on Cr d (orange) and I p (blue) orbitals.

involving t_{2g}. When the spin orientation is out of plane (i.e., the preferable direction of Cr magnetic moments in bulk CrI_3), π bonding cannot occur between t_{2g} and spin-orbit entangled $j = 1/2$ ligand states [18], leaving superexchange σ hopping as the preferred path. The e_g orbital occupation due to hybridization is certainly low compared to the t_{2g}; however, as argued by Stavropoulos *et al.* [63], the interaction given by e_g paths in the presence of heavy ligand SOC and strong Hund's coupling is expected to drive the system into a FM state. The upshift of the I $5p$ bands at -2 eV that we experimentally observe [Figs. 4(c) and 4(d)] is precisely the signature of Hund's energy gain manifesting on the ligand site, similarly to the mediation of the exchange via Te hybridized bonding in $CrGeTe_3$ [64]. Hund's on-site energy is thus minimized, stabilizing parallel spins as the ground-state configuration [65]. As a result, it is the hybridization between Cr e_g and I p orbitals in the presence of strong Hund's coupling that allows the stabilization of a FM ground state in CrI_3.

In any case, we note that the hybridized superexchange picture does not exclude contributions from other mechanisms, e.g., t_{2g}-e_g hopping, which is also expected to contribute to the FM exchange [66,67].

IV. CONCLUSIONS

In summary, we presented a combined experimental and theoretical study of the orbital structure of CrI_3, and its interplay with the emergence of long-range magnetic order in this compound. By comparing (E,k) nonresonant and resonant ARPES spectra with DFT calculations, we were able to assess the orbital-resolved band ordering. XAS and XMCD measurements at the Cr $L_{2,3}$ and I $M_{4,5}$ edges suggest a sizable orbital mixing, with an electron count of 3.52 electrons per Cr atom from multiplet cluster calculations. By means of ARPES spectra we reveal multiple large splittings (200–400 m eV) opening in I-derived bands in the FM phase,

as well as an explicit band signature (a large ∼300 m eV upshift) of Hund's on-site energy gain. Our results confirm that the ligand-metal covalent orbital character largely supports the onset of the FM phase, and that—thanks to the orbital mixing—Hund's coupling drives the charge and magnetic order in CrI_3, providing a robust demonstration of the theory put forward in Refs. [18,63] and reinforcing CrI_3 as a Mott-Hund insulator.

The present study focuses on CrI_3 as a prototypical material, but it is realistic to hypothesize that the same principles may be generalized to other vdW magnets. In particular, the considerations on correlations and couplings at an orbital-specific level, framing the electronic/magnetic phase diagram, do not lose generality when extended to other $3d$ transition metal–based systems, whenever a source of SOC in the form of a heavy ligand is provided. Given the many structural and chemical/orbital similarities between vdW magnets, we expect that further experimental endeavors may recognize the role of orbital mixing and d-orbital electronic correlations in underpinning the magnetic properties of many of these materials.

ACKNOWLEDGMENTS

The authors gratefully thank Dr. P. Stavropoulos and Dr. F. Barantani for valuable insight and fruitful discussion. This work is financially supported by the Deutsche Forschungsgemeinschaft (DFG) within Transregio TRR 227 Ultrafast Spin Dynamics Project No. B07, the Max Planck Society, and BERLIN QUANTUM, an initiative endowed by the Innovation Promotion Fund of the city of Berlin. We thank the European Synchrotron Radiation Facility (Proposals No. ih-hc-3612 and No. ih-hc-3640) and the Elettra Synchrotron for provision of beamtime; we also thank D. Betto for assistance in using beamline ID32, and J. Fujii for assistance in using beamline APE-LE. G.P. acknowledges support from Progetto PRIN 2022 "BEST-WIN" PNRR Next Generation EU–CUP B53D23004530006, and from PNRR-MUR Project No. PE0000023-NQSTI. S.P. acknowledges partial financial support by the Next-Generation-EU program via the PRIN-2022 SORBET (Grant No. 2022ZY8HJY). S.S. acknowledges financial support from the Vinča Institute, provided by the Ministry of Science, Technological Development and Innovation of the Republic of Serbia through Contract No. 451-03-33/2026-03/200017. Computational resources and support were provided by CINECA under the ISCRA initiative, through the projects ISCRA-B HP10BA00W3 and ISCRA-C HP10C6WZ1O. S.S. and S.P. acknowledge support from the Ministry of Foreign Affairs of Italy and the Ministry of Science, Technological Development, and Innovation of Serbia through the bilateral project "Van der Waals Heterostructures for Altermagnetic Spintronics," realized under the executive program for scientific and technological cooperation between the two countries. This work was partially performed in the framework of the NFFA-SPRINT facility, within the project DFM.AD006.324 NFFA, Grant No. CUP B91J12000310001.

T.P., A.D.V., and R.E. conceived the research project. A.D.V., T.P., and R.S. performed the experiments. N.B.B. and I.V. provided and supported access to synchrotron facilities. A.D.V. analyzed the experimental data. DFT calculations were conducted by S.S. under the supervision of S.P. R.S. developed the code and performed multiplet cluster calculations. L.R. participated in maintaining and running the experimental apparatus. R.E., M.W., and G.P. provided funding and scientific supervision for the experiments. A.D.V. and S.S. wrote the manuscript, with contributions from all coauthors.

DATA AVAILABILITY

The data that support the findings of this article are openly available [68].

APPENDIX: DFT METHODS

1. DFT modeling of the paramagnetic state

The magnetic anisotropy in a CrI_3 monolayer favors the out-of-plane magnetization direction. Therefore, we modeled the FM state with Cr magnetic moments of $3\mu_B$ aligned out of plane and parallel to each other. On the other hand, modeling the PM state is not trivial within the DFT approach. For this cause we used the *s*SQS approach for binary alloys [36] where instead of having two atomic types A and B like in binary alloys, we have two spin types distributed over a honeycomb lattice of Cr atoms. In particular, we constructed a $3 \times 3 \times 1$ supercell and used the ICET tool [37] to distribute nibe spin-up and nine spin-down moments in a quasirandom fashion over 18 Cr atoms. SQS structures optimally approximate random alloys by matching the correlation functions of truly random systems up to the nth nearest-neighbor shell, providing the closest structural representation for computational modeling of disordered solid solutions. This approach ensures that CrI_3 has zero net magnetization while suppressing long-range magnetic order. Note that a similar approach was used in Ref. [69] to model the PM state in the same compound. It should be noted that DFT is a zero-temperature theory, which inherently limits its ability to fully describe the physical properties of the magnetic system in the real PM phase at higher temperatures. In this regard, the DFT-simulated PM state represents an approximation where Cr magnetic moments retain their magnitude ($3\mu_B$), while the whole structure exhibits zero net magnetization and lacks long-range magnetic order.

2. Calculation of the spectral function

The spectral function, calculated with the supercell, is unfolded to the unit cell to facilitate comparison with ARPES data. The unfolding procedure is performed using the postprocessing package BANDS4VASP [38] where the spectral function is defined as $A(\mathbf{k}, E) = \sum_m P_{\mathbf{K}m}(\mathbf{k})\delta(E - E_m)$, where $\mathbf{k}$ ($\mathbf{K}$) is the wave vector in the BZ of the unit cell (supercell) and $P_{\mathbf{K}m}(\mathbf{k})$ projects the supercell eigenstates $|\mathbf{K}m\rangle$ onto the unit-cell eigenstates $|\mathbf{k}n\rangle$. By calculating the spectral function rather than just the band structure, we can identify which $\mathbf{k}$-resolved states vanish due to magnetic disorder and which remain robust. This approach directly reveals how magnetic disorder affects the electronic structure in different energy ranges and different regions of the BZ.

3. The choice of Hubbard and Hund parameters

In the work of Haddadi *et al.* [70], it is demonstrated that the PBEsol exchange-correlation functional provides a closer-to-experiments description of the electronic bands of CrI_3 compared to the PBE functional. We note that some kind of on-site energy correction is expected in CrI_3, as the insulating ground state, despite the partially filled Cr $3d$ orbital, indicates a Mott-Hubbard-driven stabilization of a band gap [71]. Therefore, we adopted the DFT+U approach as introduced by Liechtenstein *et al.* [34] and tested several combinations of (U, J) values, with U ranging from 1 to 3 eV and J from 0.6 to 0.9 eV. Spectral function plots for different (U, J) values are presented in the Supplemental Material, Fig. S6. As the main criterion, we examined how the most prominent Cr $3d$ bands calculated with DFT + U in the PM state reproduce those measured with ARPES at 300 K. Ultimately, we decided to use Hubbard $U = 1.3$ eV and Hund $J = 0.9$ eV. This particular set of (U, J) values, besides providing good overall fit of ARPES data, allows us to strike a balance between the findings of Stavropoulos *et al.* [63], who argue that a finite Hund coupling J is essential for stabilizing ferromagnetic order in CrI_3, and the results of Haddadi *et al.* [70], which demonstrate that the PBEsol functional with a small Hubbard U provides good agreement overall with experimental electronic structure data. As argued in Ref. [70], the agreement between the DFT-calculated band structure and ARPES data further improves when two distinct Hubbard U parameters are used for the spin-up and spin-down channels, though we ultimately decided to use a single U for both channels. We also note that varying J in the range from 0.6 to 0.9 eV has minimal effect on the calculated spectral function.

[1] N. Samarth, Magnetism in flatland, Nature (London) **546**, 216 (2017).

[2] M. Gibertini, M. Koperski, A. Morpurgo, and K. Novoselov, Magnetic 2D materials and heterostructures, Nat. Nanotechnol. **14**, 408 (2019).

[3] S. Kajale, J. Hanna, K. Jang, and D. Sarkar, Two-dimensional magnetic materials for spintronic applications, Nano Res. **17**, 743 (2024).

[4] A. Hoffmann and S. D. Bader, Opportunities at the frontiers of spintronics, Phys. Rev. Appl. **4**, 047001 (2015).

[5] D. Go, D. Jo, C. Kim, and H.-W. Lee, Intrinsic spin and orbital hall effects from orbital texture, Phys. Rev. Lett. **121**, 086602 (2018).

[6] E. Vedmedenko, R. Kawakami, D. Sheka, P. Gambardella, A. Kirilyuk, C. Hirohata, A. Binek, O. Chubykalo-Fesenko, S. Sanvito, B. Kirby, J. Grollier, K. Everschor-Sitte, T. Kampfrath, C.-Y. You, and A. Berger, The 2020 magnetism roadmap, J. Phys. D: Appl. Phys. **53**, 453001 (2020).

[7] P. P. Stavropoulos, D. Pereira, and H.-Y. Kee, Microscopic mechanism for a higher-spin Kitaev model, Phys. Rev. Lett. **123**, 037203 (2019).

[8] W. He, J. Sears, F. Barantani, T. Kim, J. W. Villanova, T. Berlijn, M. Lajer, M. A. McGuire, J. Pelliciari, V. Bisogni, S. Johnston, E. Baldini, M. Mitrano, and M. P. M. Dean, Dispersive dark excitons in van der Waals ferromagnet CrI_3, Phys. Rev. X **15**, 011042 (2025).

[9] C. A. Occhialini, L. Nessi, Luis G. P. Martins, A. K. Demir, Q. Song, V. Hasse, C. Shekhar, C. Felser, K. Watanabe, T. Taniguchi, V. Bisogni, J. Pelliciari, and R. Comin, Spin-forbidden excitations in the magneto-optical spectra of CrI_3 tuned by covalency, Phys. Rev. X **15**, 031005 (2025).

[10] C. Gong, L. Li, Z. Li, H. Ji, A. Stern, Y. Xia, T. Cao, W. Bao, C. Wang, Y. Wang, Z. Qiu, R. Cava, S. Louie, J. Xia, and X. Zhang, Discovery of intrinsic ferromagnetism in two-dimensional van der waals crystals, Nature (London) **546**, 265 (2017).

[11] B. Huang, G. Clark, E. Navarro-Moratalla, D. Klein, R. Cheng, K. Seyler, D. Zhong, E. Schmidgall, M. McGuire, D. Cobden, W. Yao, D. Xiao, P. Jarillo-Herrero, and X. Xu, Layer-dependent ferromagnetism in a van der Waals crystal down to the monolayer limit, Nature (London) **546**, 270 (2017).

[12] D. Soriano, M. Katsnelson, and J. Fernández-Rossier, Magnetic two-dimensional chromium trihalides: A theoretical perspective, Nano Lett. **20**, 6225 (2020).

[13] S. Jiang, J. Shan, and K. Mak, Electric-field switching of two-dimensional van der Waals magnets, Nat. Mater. **17**, 406 (2018).

[14] B. Huang, G. Clark, D. Klein, D. MacNeill, E. Navarro-Moratalla, K. Seyler, N. Wilson, M. McGuire, D. Cobden, D. Xiao, W. Yao, P. Jarillo-Herrero, and X. Xu, Electrical control of 2D magnetism in bilayer CrI_3, Nat. Nanotechnol. **13**, 544 (2018).

[15] S. Jiang, L. Li, Z. Wang, K. Mak, and J. Shan, Controlling magnetism in 2D CrI_3 by electrostatic doping, Nat. Nanotechnol. **13**, 549 (2018).

[16] S. Jiang, L. Li, Z. Wang, J. Shan, and K. Mak, Spin tunnel field-effect transistors based on two-dimensional van der Waals heterostructures, Nat. Electron **2**, 159 (2019).

[17] D. Soriano and M. I. Katsnelson, Magnetic polaron and antiferromagnetic-ferromagnetic transition in doped bilayer CrI_3, Phys. Rev. B **101**, 041402(R) (2020).

[18] D.-H. Kim, K. Kim, K.-T. Ko, J. H. Seo, J. S. Kim, T.-H. Jang, Y. Kim, J.-Y. Kim, S.-W. Cheong, and J.-H. Park, Giant magnetic anisotropy induced by ligand *LS* coupling in layered Cr compounds, Phys. Rev. Lett. **122**, 207201 (2019).

[19] A. Kundu, Y. Liu, C. Petrovic, and T. Valla, Valence band electronic structure of the van der Waals ferromagnetic insulators: VI_3 and CrI_3, Sci. Rep. **10**, 15602 (2020).

[20] A. De Vita, T. T. P. Nguyen, R. Sant, G. M. Pierantozzi, D. Amoroso, C. Bigi, V. Polewczyk, G. Vinai, L. T. Nguyen, T. Kong, J. Fujii, I. Vobornik, N. B. Brookes, G. Rossi, R. J. Cava, F. Mazzola, K. Yamauchi, S. Picozzi, and G. Panaccione, Influence of orbital character on the ground state electronic properties in the van der Waals transition metal iodides VI_3 and CrI_3, Nano Lett. **22**, 7034 (2022).

[21] M. Puppin, Y. Deng, C. W. Nicholson, J. Feldl, N. B. M. Schröter, H. Vita, P. S. Kirchmann, C. Monney, L. Rettig, M. Wolf, and R. Ernstorfer, Time- and angle-resolved photoemission spectroscopy of solids in the extreme ultraviolet at 500 kHz repetition rate, Rev. Sci. Instrum. **90**, 023104 (2019).

[22] J. Maklar, S. Dong, S. Beaulieu, T. Pincelli, M. Dendzik, Y. W. Windsor, R. P. Xian, M. Wolf, R. Ernstorfer, and L. Rettig, A quantitative comparison of time-of-flight momentum microscopes and hemispherical analyzers for time- and angle-resolved photoemission spectroscopy experiments, Rev. Sci. Instrum. **91**, 123112 (2020).

[23] A. De Vita, V. Polewczyk, G. Panaccione, and G. Vinai, Valence Modifications in Hygroscopic VI_3 degraded crystals via soft X-ray synchrotron radiation, J. Phys. Chem. C **130**, 3452 (2026).

[24] G. Panaccione *et al.*, Advanced photoelectric effect experiment beamline at elettra: A surface science laboratory coupled with synchrotron radiation, Rev. Sci. Instrum. **80**, 043105 (2009).

[25] E. A. Kraut, R. W. Grant, J. R. Waldrop, and S. P. Kowalczyk, Precise determination of the valence-band edge in x-ray photoemission spectra: Application to measurement of semiconductor interface potentials, Phys. Rev. Lett. **44**, 1620 (1980).

[26] A. D. Katnani and G. Margaritondo, Microscopic study of semiconductor heterojunctions: Photoemission measurement of the valance-band discontinuity and of the potential barriers, Phys. Rev. B **28**, 1944 (1983).

[27] See Supplemental Material at http://link.aps.org/supplemental/10.1103/bdbj-98tj for additional details on the experimental and theoretical methods, including x-ray absorption spectra across the Cr $L_{2,3}$ edges averaged between left- and right-circularly polarized photons, x-ray absorption spectra and corresponding XMCD across the I $M_{4,5}$ edges, cluster calculations of the Cr $L_{2,3}$ edges with and without hybridization, calculated values of the hybridization parameters, EDCs showing a change in bandwidth between high and low temperature, and spectral functions of a CrI_3 monolayer for different (U, J) values.

[28] K. Kummer, A. Fondacaro, E. Jimenez, E. Velez-Fort, A. Amorese, M. Aspbury, F. Yakhou-Harris, P. van der Linden, and N. B. Brookes, The high-field magnet endstation for X-ray magnetic dichroism experiments at ESRF soft X-ray beamline ID32, J. Synchrotron Radiat. **23**, 464 (2016).

[29] N. B. Brookes, F. Yakhou-Harris, K. Kummer, A. Fondacaro, J. C. Cezar, D. Betto, E. Velez-Fort, A. Amorese, G. Ghiringhelli, L. Braicovich, R. Barrett, G. Berruyer, F. Cianciosi, L. Eybert, P. Marion, P. van der Linden, and L. Zhang, The beamline ID32 at the ESRF for soft X-ray high energy resolution resonant inelastic X-ray scattering and polarisation dependent X-ray absorption spectroscopy, Nucl. Instrum. Methods Phys. Res. Sect. A **903**, 175 (2018).

[30] G. Kresse and J. Furthmüller, Efficiency of *ab-initio* total energy calculations for metals and semiconductors using a plane-wave basis set, Comput. Mater. Sci. **6**, 15 (1996).

[31] G. Kresse and J. Furthmüller, Efficient iterative schemes for *ab initio* total-energy calculations using a plane-wave basis set, Phys. Rev. B **54**, 11169 (1996).

[32] G. Kresse and D. Joubert, From ultrasoft pseudopotentials to the projector augmented-wave method, Phys. Rev. B **59**, 1758 (1999).

[33] J. P. Perdew, A. Ruzsinszky, G. I. Csonka, O. A. Vydrov, G. E. Scuseria, L. A. Constantin, X. Zhou, and K. Burke, Restoring the density-gradient expansion for exchange in solids and surfaces, Phys. Rev. Lett. **100**, 136406 (2008).

[34] A. I. Liechtenstein, V. I. Anisimov, and J. Zaanen, Density-functional theory and strong interactions: Orbital ordering in Mott-Hubbard insulators, Phys. Rev. B **52**, R5467 (1995).

[35] K. Momma and F. Izumi, *VESTA 3* for three-dimensional visualization of crystal, volumetric and morphology data, J. Appl. Crystallogr. **44**, 1272 (2011).

[36] A. Zunger, S.-H. Wei, L. G. Ferreira, and J. E. Bernard, Special quasirandom structures, Phys. Rev. Lett. **65**, 353 (1990).

[37] M. Ångqvist, W. A. Muñoz, J. M. Rahm, E. Fransson, C. Durniak, P. Rozyczko, T. H. Rod, and P. Erhart, ICET—A python library for constructing and sampling alloy cluster expansions, Adv. Theor. Simul. **2**, 1900015 (2019).

[38] D. Dirnberger, G. Kresse, C. Franchini, and M. Reticcioli, Electronic state unfolding for plane waves: energy bands, Fermi surfaces, and spectral functions, J. Phys. Chem. C **125**, 12921 (2021).

[39] B. Marfoua, I. Khan, and J. Hong, Giant spin Seebeck effect in two-dimensional ferromagnetic CrI_3 monolayer, Nanotechnology **31**, 455404 (2020).

[40] T. P. T. Nguyen, K. Yamauchi, T. Oguchi, D. Amoroso, and S. Picozzi, Electric-field tuning of the magnetic properties of bilayer VI_3: A first-principles study, Phys. Rev. B **104**, 014414 (2021).

[41] J. F. Dillon, Jr. and C. E. Olson, Magnetization, resonance, and optical properties of the ferromagnet CrI_3, J. Appl. Phys. **36**, 1259 (1965).

[42] W. Jin, H. Kim, Z. Ye, G. Ye, L. Rojas, X. Luo, B. Yang, F. Yin, J. Shih An Horng, S. Tian, Y.Fu, G. Xu, H. Deng, H. Lei, A. Tsen, K. Sun, R. He, and L. Zhao, Observation of the polaronic character of excitons in a two-dimensional semiconducting magnet CrI_3, Nat. Commun. **11**, 4780 (2020).

[43] A. Frisk, L. B. Duffy, S. Zhang, G. van der Laan, and T. Hesjedal, Magnetic X-ray spectroscopy of two-dimensional CrI_3 layers, Mater. Lett. **232**, 5 (2018).

[44] C. T. Chen, Y. U. Idzerda, H.-J. Lin, N. V. Smith, G. Meigs, E. Chaban, G. H. Ho, E. Pellegrin, and F. Sette, Experimental confirmation of the X-Ray magnetic circular dichroism sum rules for iron and cobalt, Phys. Rev. Lett. **75**, 152 (1995).

[45] W. L. O'Brien, B. P. Tonner, G. R. Harp, and S. S. P. Parkin, Experimental investigation of dichroism sum rules for V, Cr, Mn, Fe, Co, and Ni: Influence of diffuse magnetism, J. Appl. Phys. **76**, 6462 (1994).

[46] Y. Ito, T. Tochio, A. Vlaicu, D. Ohsawa, T. Mukoyama, Y. Muramatsu, R. Perera, M. Grush, T. Callcott, and E. Sherman, The contribution of the ligands around Cr to the resonant inelastic L X-ray emission spectra, J. Electron Spectrosc. Relat. Phenom. **101-103**, 851 (1999).

[47] S. O. Kucheyev, B. Sadigh, T. F. Baumann, Y. M. Wang, T. E. Felter, T. van Buuren, A. E. Gash, J. H. Satcher, Jr., and A. V. Hamza, Electronic structure of chromia aerogels from soft x-ray absorption spectroscopy, J. Appl. Phys. **101**, 124315 (2007).

[48] J. Chiou, S. Chang, W. Huang, Y. Chen, C. Hsu, Y. Hu, J. Chen, C.-H. Chen, K. Kumar, and J.-H. Guo, The characterization of Cr secondary oxide phases in ZnO films studied by X-ray spectroscopy and photoemission spectroscopy, Appl. Surf. Sci. **257**, 4863 (2011).

[49] S. B. Singh, L. T. Yang, Y. F. Wang, Y. C. Shao, C. W. Chiang, J. W. Chiou, K. T. Lin, S. C. Chen, B. Y. Wang, C. H. Chuang, D. C. Ling, W. F. Pong, M.-H. Tsai, H. M. Tsai, C. W. Pao, H. W. Shiu, C. H. Chen, H.-J. Lin, J. F. Lee, H. Yamane, N. Kosugi, *et al.*, Correlation between p -type conductivity and electronic structure of Cr-deficient $CuCr_{1-x}O_2 (x = 0–0.1)$, Phys. Rev. B **86**, 241103 (2012).

[50] G. Cristian Vásquez, D. Maestre, A. Cremades, J. Ramírez-Castellanos, E. Magnano, S. Nappini, and S. Karazhanov, Understanding the effects of Cr doping in rutile TiO_2 by DFT calculations and X-ray spectroscopy, Sci. Rep. **8**, 8740 (2018).

[51] R. Sant, A. De Vita, V. Polewczyk, G. Pierantozzi, F. Mazzola, G. Vinai, G. van der Laan, G. Panaccione, and N. B. Brookes, Anisotropic hybridization probed by polarization dependent x-ray absorption spectroscopy in VI_3 van der Waals Mott ferromagnet, J. Phys.: Condens. Matter **35**, 405601 (2023).

[52] A. De Vita, R. Sant, V. Polewczyk, G. van der Laan, T. Brookes, N.B. Kong, R. Cava, G. Rossi, G. Vinai, and G. Panaccione, Evidence of temperature-dependent interplay between spin and orbital moment in van der Waals ferromagnet VI_3, Nano Lett. **24**, 1487 (2024).

[53] C. Theil, J. van Elp, and F. Folkmann, Ligand field parameters obtained from and chemical shifts observed at the Cr $L_{2,3}$ edges, Phys. Rev. B **59**, 7931 (1999).

[54] M. Abbate, F. M. F. de Groot, J. C. Fuggle, A. Fujimori, O. Strebel, F. Lopez, M. Domke, G. Kaindl, G. A. Sawatzky, M. Takano, Y. Takeda, H. Eisaki, and S. Uchida, Controlled-valence properties of $La_{1-x}Sr_xFeO_3$ and $La_{1-x}Sr_xMnO_3$ studied by soft-X-ray absorption spectroscopy, Phys. Rev. B **46**, 4511 (1992).

[55] M. P. de Jong, I. Bergenti, V. A. Dediu, M. Fahlman, M. Marsi, and C. Taliani, Evidence for Mn^{2+} ions at surfaces of $La_{0.7}Sr_{0.3}MnO_3$ thin films, Phys. Rev. B **71**, 014434 (2005).

[56] R. Werner, C. Raisch, A. Ruosi, B. A. Davidson, P. Nagel, M. Merz, S. Schuppler, M. Glaser, J. Fujii, T. Chassé, R. Kleiner, and D. Koelle, $YBa_2Cu_3O_7/La_{0.7}Ca_{0.3}MnO_3$ bilayers: Interface coupling and electric transport properties, Phys. Rev. B **82**, 224509 (2010).

[57] D. Pesquera, A. Barla, M. Wojcik, E. Jedryka, F. Bondino, E. Magnano, S. Nappini, D. Gutiérrez, G. Radaelli, G. Herranz, F. Sánchez, and J. Fontcuberta, Strain-driven orbital and magnetic orders and phase separation in epitaxial half-doped manganite films for tunneling devices, Phys. Rev. Appl. **6**, 034004 (2016).

[58] Y. Ishida, M. Kobayashi, J.-I. Hwang, Y. Takeda, S. ichi Fujimori, T. Okane, K. Terai, Y. Saitoh, Y. Muramatsu, A. Fujimori, A. Tanaka, H. Saito, and K. Ando, X-ray magnetic circular dichroism and photoemission study of the diluted ferromagnetic semiconductor $Zn_{1-x}Cr_xTe$, Appl. Phys. Express **1**, 041301 (2008).

[59] G. Buccoliero, P. Vasconcelos Borges Pinho, M. Dos Reis Cantarino, F. Rosa, N. B. Brookes, and R. Sant, *In situ* growth and magnetic characterization of Cr Chloride monolayers, Adv. Mater. Interfaces **12**, e00229 (2025).

[60] Y. Liu and C. Petrovic, Three-dimensional magnetic critical behavior in CrI_3, Phys. Rev. B **97**, 014420 (2018).

[61] Y. Shao, B. Karki, W. Huang, X. Feng, G. Sumanasekera, J. Guo, Y. Chuang, and B. Freelon, Spectroscopic determination of key energy scales for the base Hamiltonian of chromium trihalides, J. Phys. Chem. Lett. **12**, 724 (2021).

[62] M. W. Haverkort, *Quanty* for core level spectroscopy—excitons, resonances and band excitations in time and frequency domain, J. Phys.: Conf. Ser. **712**, 012001 (2016).

[63] P. P. Stavropoulos, X. Liu, and H.-Y. Kee, Magnetic anisotropy in spin-3/2 with heavy ligand in honeycomb Mott insulators: Application to CrI_3, Phys. Rev. Res. **3**, 013216 (2021).

[64] M. D. Watson, I. Marković, F. Mazzola, A. Rajan, E. A. Morales, D. M. Burn, T. Hesjedal, G. van der Laan, S. Mukherjee, T. K. Kim, C. Bigi, I. Vobornik, M. Ciomaga Hatnean, G. Balakrishnan, and Philip D. C. King, Direct observation of the energy gain underpinning ferromagnetic superexchange in the electronic structure of $CrGeTe_3$, Phys. Rev. B **101**, 205125 (2020).

[65] S. Ivanov, J. Peacock, and S. Urazhdin, Orbital correlations in ultrathin films of late transition metals, Phys. Rev. Mater. **7**, 014404 (2023).

[66] K. W. Song and V. I. Fal'ko, Superexchange and spin-orbit coupling in monolayer and bilayer chromium trihalides, Phys. Rev. B **106**, 245111 (2022).

[67] A. Ghosh, H. J. M. Jönsson, D. J. Mukkattukavil, Y. Kvashnin, D. Phuyal, P. Thunström, M. Agåker, A. Nicolaou, M. Jonak, R. Klingeler, M. V. Kamalakar, T. Sarkar, A. N. Vasiliev, S. M. Butorin, O. Eriksson, and M. Abdel-Hafiez, Magnetic circular dichroism in the dd excitation in the van der Waals magnet CrI_3 probed by resonant inelastic X-ray scattering, Phys. Rev. B **107**, 115148 (2023).

[68] A. Devita, S. Stavrić, R. Sant, N. B. Brookes, I. Vobornik, G. Panaccione, S. Picozzi, M. Wolf, L. Rettig, R. Ernstorfer, and T. Pincelli, Dataset for the article "Orbital mixing and strong Hund's coupling stabilize spin order in the van der Waals ferromagnet CrI_3" [Data set], Zenodo (2026), https://doi.org/10.5281/zenodo.19481696.

[69] X.-Y. Chen, M.-Q. Long, and Y.-P. Wang, Paramagnetic phases of two-dimensional magnetic materials, Phys. Rev. B **102**, 214417 (2020).

[70] F. Haddadi, E. Linscott, I. Timrov, N. Marzari, and M. Gibertini, On-site and intersite Hubbard corrections in magnetic monolayers: The case of $FePS_3$ and CrI_3, Phys. Rev. Mater. **8**, 014007 (2024).

[71] L. Webster and J.-A. Yan, Strain-tunable magnetic anisotropy in monolayer $CrCl_3$, $CrBr_3$, and CrI_3, Phys. Rev. B **98**, 144411 (2018).